



## Full paper

## Highly polarized carbon nano-architecture as robust metal-free catalyst for oxygen reduction in polymer electrolyte membrane fuel cells

Jianbing Zhu<sup>a,b</sup>, Meiling Xiao<sup>a,b</sup>, Ping Song<sup>a</sup>, Jing Fu<sup>b</sup>, Zhao Jin<sup>a</sup>, Liang Ma<sup>c,\*</sup>, Junjie Ge<sup>a,\*</sup>, Changpeng Liu<sup>a</sup>, Zhongwei Chen<sup>b,\*</sup>, Wei Xing<sup>a,\*</sup>

<sup>a</sup> State Key Laboratory of Electroanalytical Chemistry, Laboratory of Advanced Power Sources, Changchun Institute of Applied Chemistry, Chinese Academy of Sciences, Changchun 130022, China

<sup>b</sup> Department of Chemical Engineering, Waterloo Institute for Nanotechnology, Waterloo Institute for Sustainable Energy, University of Waterloo, Waterloo, Ontario, Canada

<sup>c</sup> Faculty of Materials Science and Chemistry, China University of Geosciences, Wuhan 430074, China

## ARTICLE INFO

## Keywords:

Metal-free catalyst  
Active site  
Oxygen reduction reaction  
Polymer electrolyte membrane fuel cell

## ABSTRACT

Metal-free electrocatalysts have eluded widespread adoption in polymer electrolyte membrane fuel cells due to their far inferior catalytic activity than most non-precious metal-N-C counterparts (M-N<sub>x</sub>-C) for oxygen reduction reaction (ORR), despite their distinct advantages over the M-N<sub>x</sub>-C catalysts, including lower cost and higher durability. Herein, we develop a rational bottom-up engineering strategy to improve the ORR performance of a metal-free catalyst by constructing a three-dimensional ultrathin N, P dual-doped carbon nanosheet. The resultant catalyst represents unprecedented ORR performance with an onset potential of 0.91 V, half-wave potential of 0.79 V. Impressively, a maximum power output at 579 mW cm<sup>-2</sup> is generated in the fuel cell test, the best among reported metal-free catalysts and outperforms most of the M-N<sub>x</sub>-C catalysts. The outstanding catalytic performance results from the highly active polarized carbon sites which are induced by selective graphitic nitrogen and phosphorous dual doping. Our findings provide new directions for the exploration of alternatives to Pt and bring a renew interests in the metal-free catalysts.

## 1. Introduction

Polymer electrolyte membrane fuel cells (PEMFCs) are regarded as the most promising energy technology to replace the internal combustion engines as the vehicular power source [1,2]. One major obstacle impedes their wide spread application is the high cost and limited reserve of the state-of-the-art Pt-based catalysts. In this regard, great endeavors have been paid to search efficient non-precious metal catalysts (NPMCs) towards oxygen reduction reaction (ORR) [3–5]. Among the varied type of catalysts, the metal-free carbon-based materials exhibit distinct advantages over other NPMCs due to their lower cost, higher durability and simpler active site structure [6–8]. Since Gong et al. firstly reported nitrogen-doped carbon nanotube arrays as ORR catalysts in Science [5], optimizing carbon nanostructure (1D nanotube [5,9,10], 2D nanosheet [11], 3D nanostructure [12,13]) and modulating the doping elements (N, S, P, B, F or multiple atom doping [14–25]) have been majorly adopted to boost the catalytic performance. The regulation in carbon nanostructure addresses the accessible active site density, electronic conductivity, as well as the mass transfer properties of the catalysts [26–30]. Meanwhile, the doping

elements modulate the intrinsic activity by altering the charge and spin density of carbon atoms [31–35].

Despite the enormous progress achieved, two obstacles remain for further development of the metal free catalysts: First, their catalytic performance in acid media for PEMFCs is still far away from satisfactory although a variety of heteroatoms-doped carbon materials were reported due to the low active site density and poor leached intrinsic activity. This has led to a judgement that transition metals (the M-N<sub>x</sub>-C type catalysts) are indispensable for the nonprecious catalysts in acidic solution, which greatly discourages the search for efficient acidic metal free ORR catalysts. Second, the understanding in the real active sites is also obscured due to the non-uniform structure, which hinders further rational design of high-performance metal-free electrocatalysts. Obviously, only when the intrinsic activity (doping functionalities), the activity unleashing issues (the tune in carbon structure) and the identification of active site are simultaneously addressed can metal free catalysts become truly promising towards PEMFCs applications.

Herein, we aimed at improving the metal-free catalysts' performance through combining the electronic modulation with nanostructure

\* Corresponding authors.

E-mail addresses: [liangma@cug.edu.cn](mailto:liangma@cug.edu.cn) (L. Ma), [gejj@ciac.ac.cn](mailto:gejj@ciac.ac.cn) (J. Ge), [zhwchen@uwaterloo.ca](mailto:zhwchen@uwaterloo.ca) (Z. Chen), [xingwei@ciac.jl.cn](mailto:xingwei@ciac.jl.cn) (W. Xing).

engineering strategy, which is achieved by constructing a series of N, P dual-doped carbon (NPC) materials featured with adjustable 3D porous nanosheet structure. Phosphorus is intentionally introduced to boost the intrinsic activity via electronic modulation effect, where its promotional effect is validated by a combination of ultraviolet photoelectron spectroscopy (UPS) analysis and density functional theory (DFT) calculation. The energy barrier of the  $O_{2(ads)}$  hydrogenation to form  $OOH_{(ads)}$  is reduced due to the significantly lowered local work function of active carbon atoms neighborhood the N, P dopants. Meanwhile, nanostructure engineering ensures the successful activity manifestation of these novel active sites, confirmed by enlarged current density. As a result, the N, P dual-doped carbon nanosheet catalyst presents unprecedented catalytic activity in acid media among the metal-free catalysts, i.e., an onset potential of 0.91 V, and half-wave potential of 0.79 V, outperforming most of the reported M-N<sub>x</sub>-C catalysts. The superb ORR performance of the derived catalyst is also confirmed by H<sub>2</sub>/O<sub>2</sub> single cell test. Our study not only paves new ways for the design of NPMCs, but also verifies the comparable contribution of metal-free active site structure to commonly recognized M-N<sub>x</sub> site, pushing the field one step ahead.

## 2. Materials and methods

### 2.1. Reagents

Melamine, diphenylphosphinic acid and zinc chloride were purchased from Aladdin Company. 5 wt% Nafion ionomer was obtained from Aldrich. Perchloric acid was purchased from Alfa Aesar. Commercial state-of-the-art 20 wt% Pt/C (Johnson Matthey Company, HiSPEC™ 3000) was used as the benchmark for comparison and was denoted as Pt/C. Ultrapure water (Millipore, 18.2 MΩ cm) was used throughout all experiments.

### 2.2. Preparation of materials

The melamine–diphenylphosphinic acid complex crystals (MDPCC) with adjustable N/P ratios were synthesized by a wet chemistry method. For a typical synthesis of MDPCC with N/P ratio of 4, melamine (2.52 g) and ultrapure water (100 mL) were added into a 250 mL single-necked, round-bottomed flask. Then flask was transferred into an oil bath and heated at 100 °C under stirring. After the solution became clear diphenylphosphinic acid (1.09 g) was added into the solution and the mixture was allowed to react at 100 °C for 3 h. Finally the solution was evaporated to dryness and obtained the precursor.

The N, P co-doped catalyst was synthesized by pyrolyzing melamine–diphenylphosphinic acid complex crystals at the target temperature. Typically, 2.0 g MDPCC was placed in a quartz boat and then pyrolyze at 1100 °C under N<sub>2</sub> atmosphere for 1 h, with a heating rate of 2 °C/min. The obtained material was denoted as NPC-X-1100. For the NPC-4-1100-Zn sample, 2.0 g MDPCC precursor mixed with 500 mg ZnCl<sub>2</sub>, then pyrolyzing with the same procedure described above.

### 2.3. Physical characterization

Scanning electron microscopy (SEM) measurements were performed with an XL 30 ESEM FEG field emission scanning electron microscope. Transmission electron microscopy (TEM), high resolution transmission electron microscopy (HRTEM), high-annular dark-field scanning transmission electron microscopy (STEM) and element mapping analysis were conducted on Philips TECNAI G2 electron microscope operating at 200 kV. X-ray diffraction (XRD) measurements were performed with a PW-1700 diffractometer using a Cu K<sub>α</sub> ( $\lambda = 1.5405 \text{ \AA}$ ) radiation source (Philips Co.). Raman spectra were collected on a J-Y T64000 Raman spectrometer with 514.5 nm wavelength incident laser light. The textural and morphological features of the various carbon supports and catalysts prepared were determined by nitrogen physisorption at 77 K in a Micromeritics ASAP 2020. Textural properties such as the

specific surface area pore volume and pore size distribution were calculated from each corresponding nitrogen adsorption–desorption isotherm, applying the Brunauer–Emmett–Teller (BET) equation and the Barrett–Joyner–Halenda (BJH). X-ray photoelectron spectroscopy (XPS) measurements were carried out on Mg K<sub>α</sub> radiation source (Kratos XSAM-800 spectrometer). The bulk compositions were evaluated by inductively coupled plasma optical emission spectrometer (X Series 2, Thermo Scientific USA).

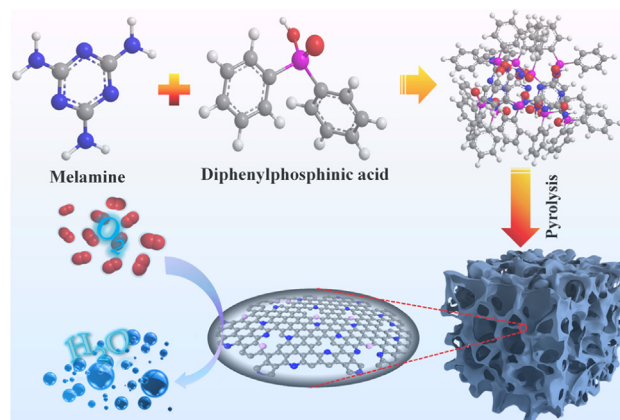
### 2.4. Electrochemical measurement

All electrochemical measurements were conducted in a conventional three-electrode cell at room temperature (~25 °C) using the 750E Bipotentiostat (CH Instruments). Non-noble metal catalyst ink was prepared by ultrasonically dispersing 5 mg catalyst in a suspension containing 50  $\mu\text{L}$  Nafion (5 wt%) solution and 950  $\mu\text{L}$  ethanol, while Pt/C catalyst (20 wt% Pt on Vulcan XC-72 carbon, Johnson Matthey) ink was prepared by dispersing 5 mg catalyst ultrasonically in a mixture solution containing 50  $\mu\text{L}$  Nafion (5 wt%) solution, 550  $\mu\text{L}$  isopropanol and 400  $\mu\text{L}$  Milli-Q water. The catalyst film coated electrode was obtained by dispersing the catalyst ink on a glassy carbon rotating ring-disk electrode followed by drying in air. The catalyst loadings on RRDE were 0.4 mg cm<sup>-2</sup> for NPC-X-T catalysts and 40  $\mu\text{g}_{\text{Pt}}$  cm<sup>-2</sup> for Pt/C catalyst. The ORR stability was investigated by continuous potential cycling in oxygen-saturated 0.1 M HClO<sub>4</sub> solution between 0.6 V and 1.05 V with the scan rate at 0.1 V s<sup>-1</sup>. And after 10, 000 cycles, the ORR steady-state polarization measurements were conducted in O<sub>2</sub>-saturated 0.1 M HClO<sub>4</sub> solution with scanning rates of 5 mV/s and rotation rate at 1600 rpm.

## 3. Results and discussion

The porous metal-free NPC catalysts were synthesized via a template-free process as illustrated in Scheme 1. The melamine and diphenylphosphinic acid were firstly allowed to cooperatively assemble into melamine–diphenylphosphinic acid complex crystals (MDPCC), confirmed by the Fourier Transform Infrared Spectroscopy (FTIR) together with <sup>31</sup>P NMR spectra (Figs. S1–3). Subsequently, the MDPCC underwent a one-step pyrolysis to yield the final NPC catalysts. The precursor was pyrolyzed under various temperatures (800–1100 °C) and catalysts with different melamine/diphenylphosphinic acid feeding ratios (N/P ratios) were synthesized, with resultant samples labeled as NPC-X-T (X represents the N/P ratios in the precursor, T represents pyrolytic temperature). Furthermore, the microstructures of these NPC-X-T catalysts were further optimized by co-pyrolyzing the MDPCC precursor in the presence of ZnCl<sub>2</sub> (NPC-4-1100-Zn).

The morphology and structure of the as-synthesized materials were examined by scanning electron microscopy (SEM) and transmission electron microscopy (TEM) images. First, increasing the pyrolysis



Scheme 1. Schematic illustration of the synthesis of NPC-X-T electrocatalysts.

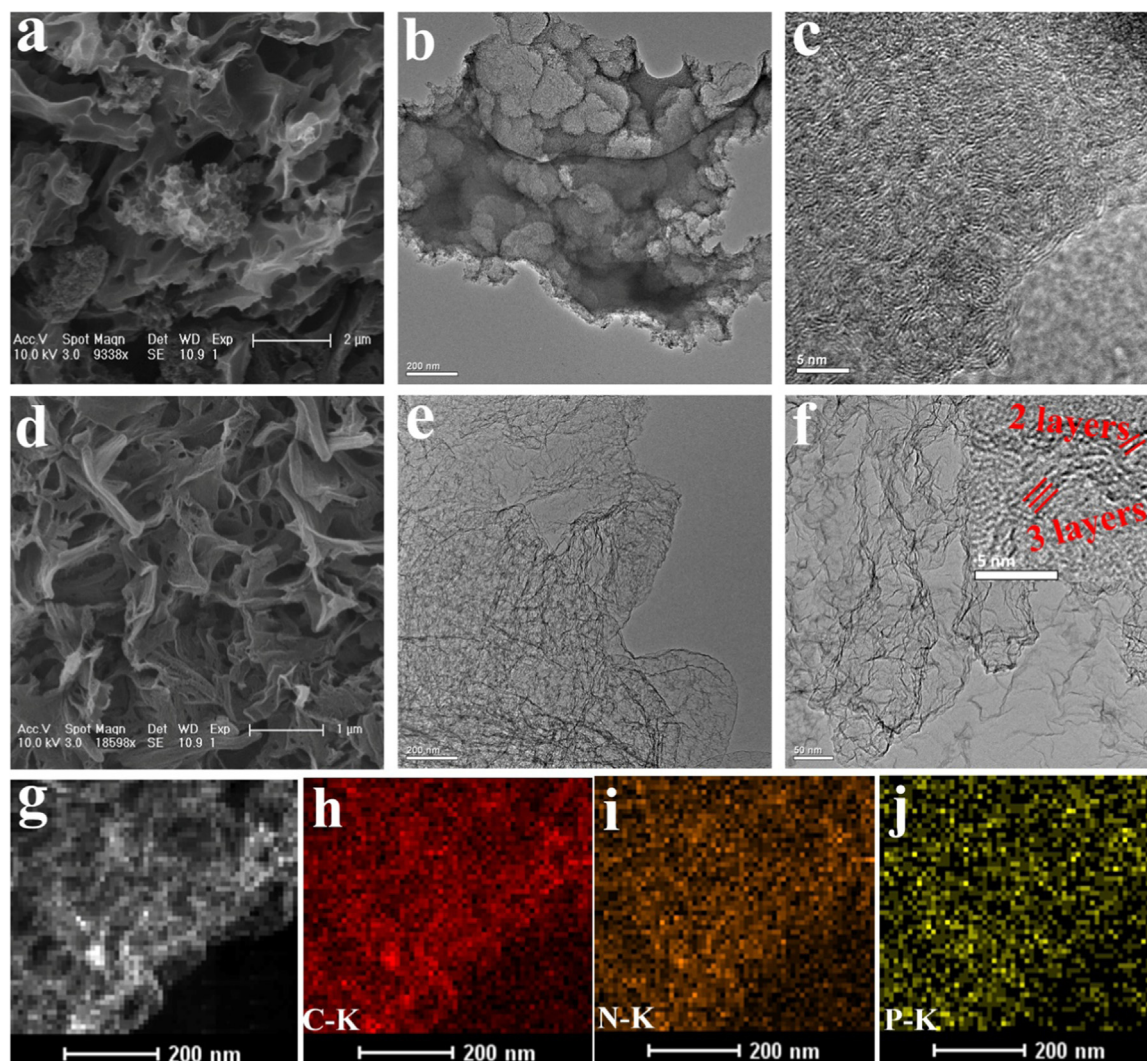


**Fig. 1.** (a) SEM, (b) TEM, (c) HRTEM images of NPC-4-1100; (d) SEM, (e) TEM and (f) HRTEM images and (g-j) corresponding the elements maps of NPC-4-1100-Zn, (h) C-K, (i) N-K, (j) P-K.

temperature results in structure evolution from solid block morphology (NPC-4-800) into fluffy three-dimensional nanosheet structure (Fig. 1 and Fig. S4), with NPC-4-1100 achieving the most uniform and porous structure. N and P were both successfully doped into carbon skeletons throughout the whole carbon matrix, as shown in Fig. S5. Besides, higher pyrolysis temperature leads to higher graphitization degree, as evidenced by clearer lattice fringes observed from the HRTEM and decreased  $I_d/I_g$  value in Raman spectra (Fig. S6). Second, we investigated the influence of N/P ratio in the precursor on the microstructure of the pyrolytic materials. As shown in Fig. S7, increasing the melamine ratio results in structure transformation from solid block aggregates (NPC-1-1100 and NPC-2-1100) into 3D porous nanosheet structure (NPC-4-1100 and NPC-6-1100), caused by the massive gas generated from melamine decomposition into carbon nitride gases (e.g.  $C_2N_2^+$ ,  $C_3N_2^+$ ,  $C_3N_3^+$ ). Third, the structure of the NPC-4-1100 catalysts (the one with most uniform pore structure) can be further tuned by adding  $ZnCl_2$  into the precursor before pyrolysis. The resultant NPC-4-1100-Zn catalyst represents a three-dimensional macroporous structure, where the walls (Fig. 1d-j) exhibit well defined graphitic structure consisting of 2–4 graphene layers, much thinner than the NPC-4-1100 catalyst (inset Fig. 1f). The highly graphitized feature and the porous structure guarantee the final NPC-4-1100-Zn with good electronic conductivity, active site accessibility, and fluent mass transfer.

We then investigated the surface area and pore structure of the

synthesized catalysts through Brunauer-Emmett-Teller (BET) technique. The  $N_2$  adsorption–desorption results (Fig. 2a and Figs. S8 and S9) demonstrate type IV isotherm for all the catalysts. Combining with the pore size distribution analysis, the catalysts are confirmed to exhibit hierarchical porous structure; where micropores ( $< 2$  nm) and mesopores are simultaneously present (Fig. 2b and Figs. S8 and S9). For all the NPC-X-T catalysts, higher pyrolytic temperature and larger N/P ratio leads to enlargement in surface areas, with the NPC-4-1100 catalyst exhibits the highest surface area of  $1698 \text{ m}^2 \text{ g}^{-1}$  and largest pore volume of  $1.92 \text{ cm}^3 \text{ g}^{-1}$  (Fig. S10 and Table S1). The introduction of Zn (NPC-4-1100-Zn) leads to further enhanced surface area ( $2048 \text{ m}^2 \text{ g}^{-1}$ ) and pore volume ( $2.79 \text{ cm}^3 \text{ g}^{-1}$ , Fig. S10), which exceeds that of NPC-4-1100 and most of the reported heteroatom-doped carbon materials [36–39]. The X-ray photoelectron spectroscopy (XPS) was adopted to characterize the surface structure of the catalysts. The deconvoluted high resolution N 1s spectra (Fig. 2c, d and Figs. S11 and S12) show the concurrent presence of pyridinic N (398.5 eV), graphitic N (401.3 eV), and pyrrolic N (399.5 eV). The P 2p spectra were deconvoluted into two peaks at 132.9 eV (P-C) and 133.8 eV (P-O), confirming the successful doping of P and the formation of P conjugated aromatic C rings (Fig. 2c, d and Figs. S11 and S12). No signals at around 402.2 eV for N–P bonding can be found, indicating the isolated N and P species in the carbon network. The surface N and P doping concentrations are found to decrease with increase in pyrolysis temperature (Fig. S13 and Table

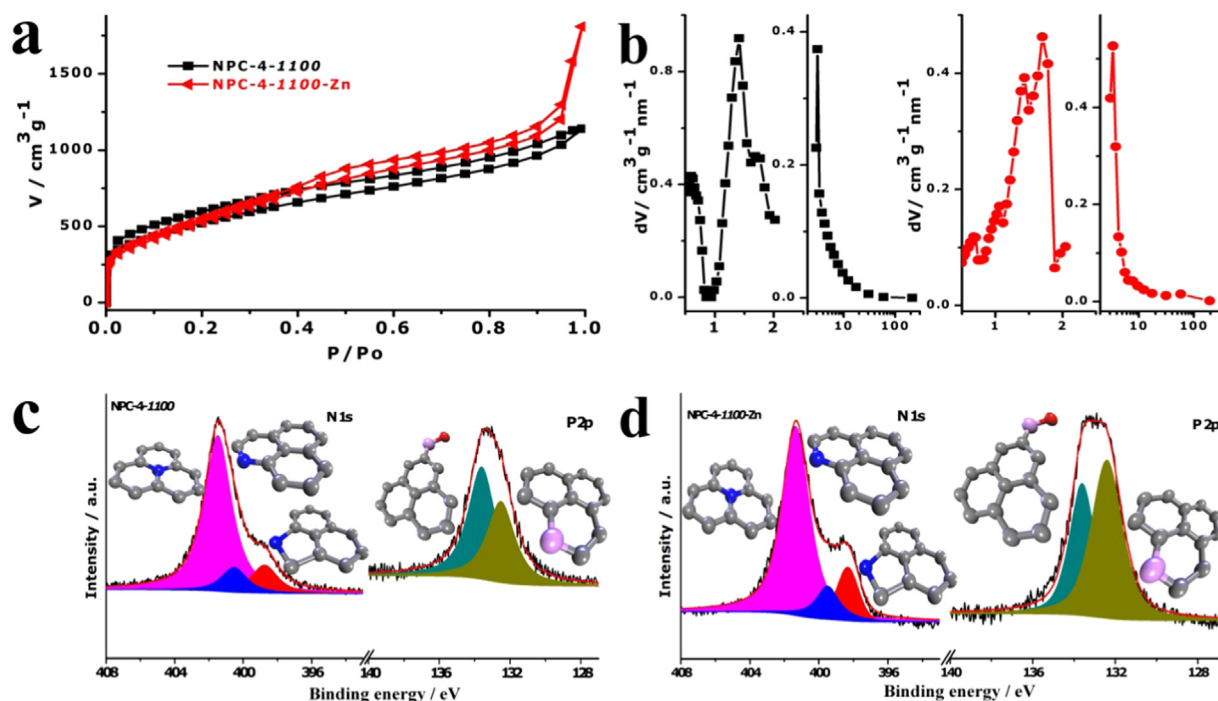


Fig. 2. (a)  $N_2$  adsorption–desorption isotherms and (b) the corresponding pore size distribution curves for NPC-4-1100 and NPC-4-1100-Zn catalysts; High-resolution N 1s and P 2p XPS spectra for (c) NPC-4-1100, (d) NPC-4-1100-Zn catalysts.

S2), and the respective concentrations of N and P are also well tuned by varying N/P feeding ratios (Fig. S13 and Table S2). Of all the NPC-X-T catalysts, the NPC-4-1100 represents the most balanced N (5.90 at%) and P doping levels (2.14 at%), which is considered to be beneficial for ORR, provided N and P both promote the catalytic process. It is noted that while the final NPC-4-1100-Zn represents comparable P and N doping levels with NPC-4-1100, the P 2p spectra shows a higher proportion of P-C species than P-O, suggesting the promotional effect of Zn in the formation of P conjugated aromatic C rings.

The electrocatalytic performance of the catalysts was evaluated using rotating ring-disk electrode (RRDE) technique in  $O_2$ -saturated 0.1 M  $HClO_4$  solution and compared with the commercial Pt/C catalysts (Johnson Matthey, 20% Pt). A clear impact of synthetic condition on both onset potential and limiting current is observed, as illustrated in Fig. 3. Specifically, the NPC-4-900, NPC-4-1000, and NPC-4-1100 represent onset potentials of 0.82, 0.85, and 0.91 V, in sequence, while the NPC-4-800 shows almost no ORR activity with only a small current at ultra-high over potential ( $\sim 0.5 \text{ mA cm}^{-2}$  at 0.1 V vs. RHE, Fig. 3a). The main reason for the ultra-low ORR activity on NPC-4-800 might be due to the insufficient electronic conductivities of NPC-4-800 (because of the low graphitization degree), as revealed by the quasi-reversible  $[Fe(CN)_6]^{3-/4-}$  redox test (Fig. S14). Meanwhile, the ORR 4-electron pathway selectivity enhanced with increasing pyrolytic temperature, as evidenced by the decreased  $H_2O_2$  yield from Fig. S15, which corresponds to the electron transfer number of 3.76, 3.81 and 3.95 for NPC-4-900, NPC-4-1000, and NPC-4-1100 (Figs. S15b and S16), respectively. As for the catalysts with different

N/P ratios, the NPC-4-1100 catalyst represents the best performance with half-wave potential locates at 0.775 V as well as excellent stability (Fig. S17). In comparison, while NPC-1-1100 and NPC-2-1100 catalysts are unsuccessful in reaching the diffusion limited current density plateau, the NPC-6-1100 catalyst exhibits a 75 mV negative shift in half-wave potential ( $E_{1/2} = 0.70 \text{ V}$ , Fig. 3b). The RRDE measurements further confirm the lowered charge transfer number of NPC-1-1100 and NPC-2-1100 catalysts and the four-electron ORR process ( $n > 3.85$ ) on the NPC-6-1100 catalyst (Figs. S15c, d and S18). It is noted that although quite different behaviors were observed in the mixed kinetic-diffusion control region and diffusion

limited current density plateau, almost all the NPC-X-1100 catalysts showed similar onset potential, indicating the NPC-X-1100 catalysts shared the same active site at different active site densities. Additionally, NPC-4-1100 catalyst exhibited significantly enhanced ORR activity compared with the N-doped C and P-doped C catalysts (Fig. S19), further verified the synergetic effect between N and P dopants.

Of particular interest is the NPC-4-1100-Zn catalyst, which performs even better than NPC-4-1100, with  $E_{1/2}$  at 0.79 V (15 mV positive shift) and charge transfer number at 3.95 ( $\sim 1\% H_2O_2$  in all potential region) obtained (Fig. 3c-e and Fig. S20). This result not only corresponds to the highest ORR performance ever reported for metal free catalysts, but also exceeds most of the M-N<sub>x</sub>-C catalysts (Table S3) and only shows a 50 mV negative shift in  $E_{1/2}$  compared with the state-of-the-art Pt/C catalysts ( $E_{1/2} = 0.845 \text{ V}$ ). The analysis of Tafel slopes for NPC-4-1100 (64.5 mV/dec), NPC-4-1100-Zn (56.9 mV/dec) and Pt/C (63.7 mV/dec) catalysts (Fig. 3d) revealed the similar ORR kinetic process on these electrodes, where the transfer of the first electron from the electrode to  $O_2$  is the rate limiting step. The ORR stability of NPC-4-1100-Zn catalyst was also evaluated using an accelerated durability test protocol by cycling the catalysts between 0.6 and 1.0 V at 100 mV/s in  $O_2$ -saturated electrolyte. As shown in Fig. 3g, after 10,000 cycles, the NPC-4-1100-Zn catalyst showed 16 mV negative shift in half-wave potential, comparable to that of Pt/C catalyst (15 mV, Fig. 3h) and nearly unchanged Tafel slope (Fig. S21). To further validate the excellent ORR performance of NPC-4-1100-Zn catalyst, single cell test was conducted. As shown in Fig. 3i, the open circuit voltage of the single cell is 0.905 V, which is consistent with results from the RRDE measurements, and the maximum power output was  $579 \text{ mW cm}^{-2}$  for the NPC-4-1100-Zn much better than that of NPC-4-1100 catalyst ( $393 \text{ mW cm}^{-2}$ ). We further conducted durability test at a constant cell voltage of 0.5 V (Fig. S22). As can be seen, it delivered a decent stability performance by showing only ca. 21.5% loss of the initial current over 72 h of operation, demonstrating excellent durability of NPC-4-1100-Zn cathode electrocatalyst. This result suggests the highly promising future of the metal free catalyst to be utilized in real PEMFC system.

Based on the fact that metal-free N doped carbon-based ORR catalysts exhibiting onset potential over 0.8 V in acidic solution has never

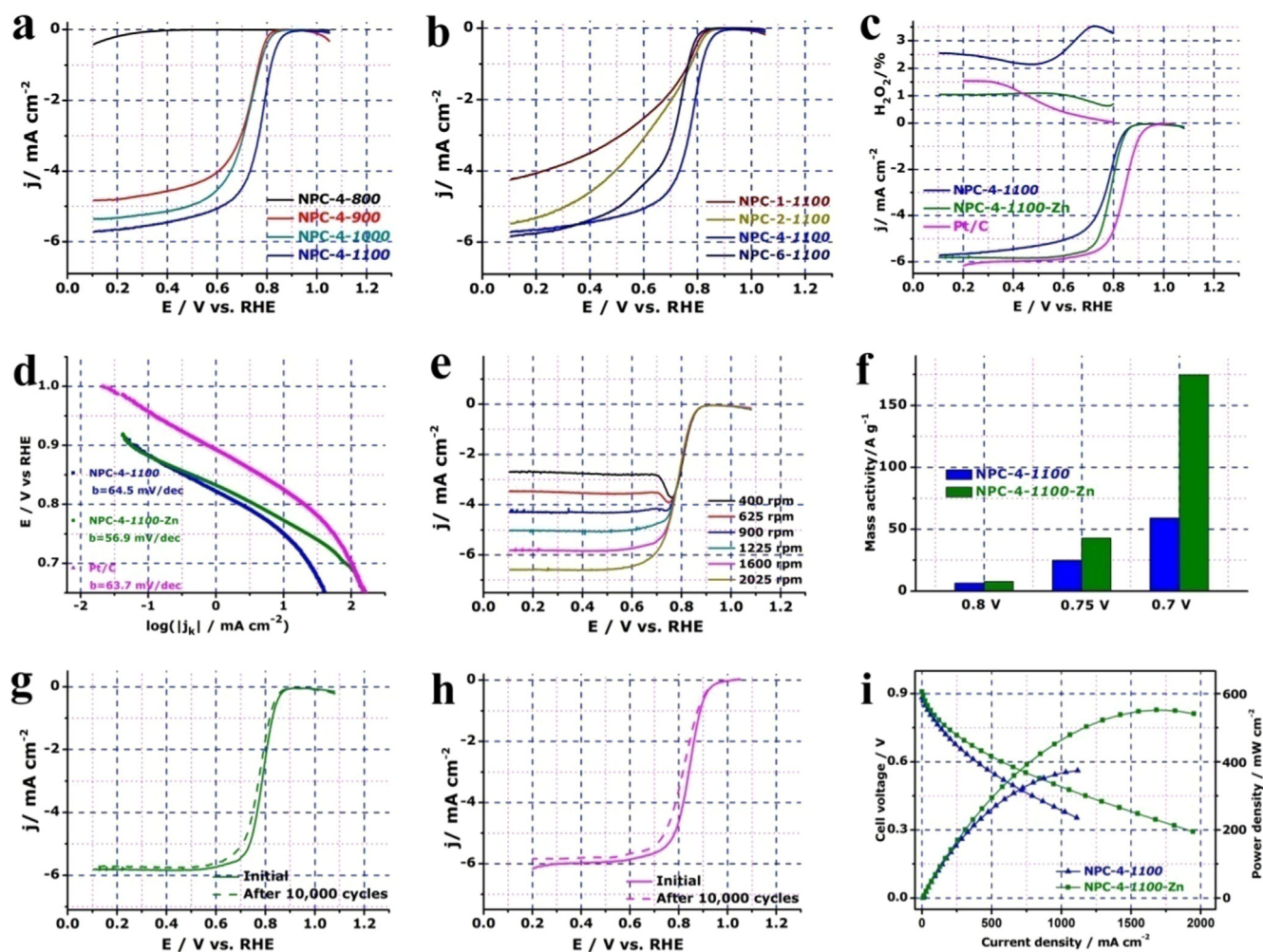
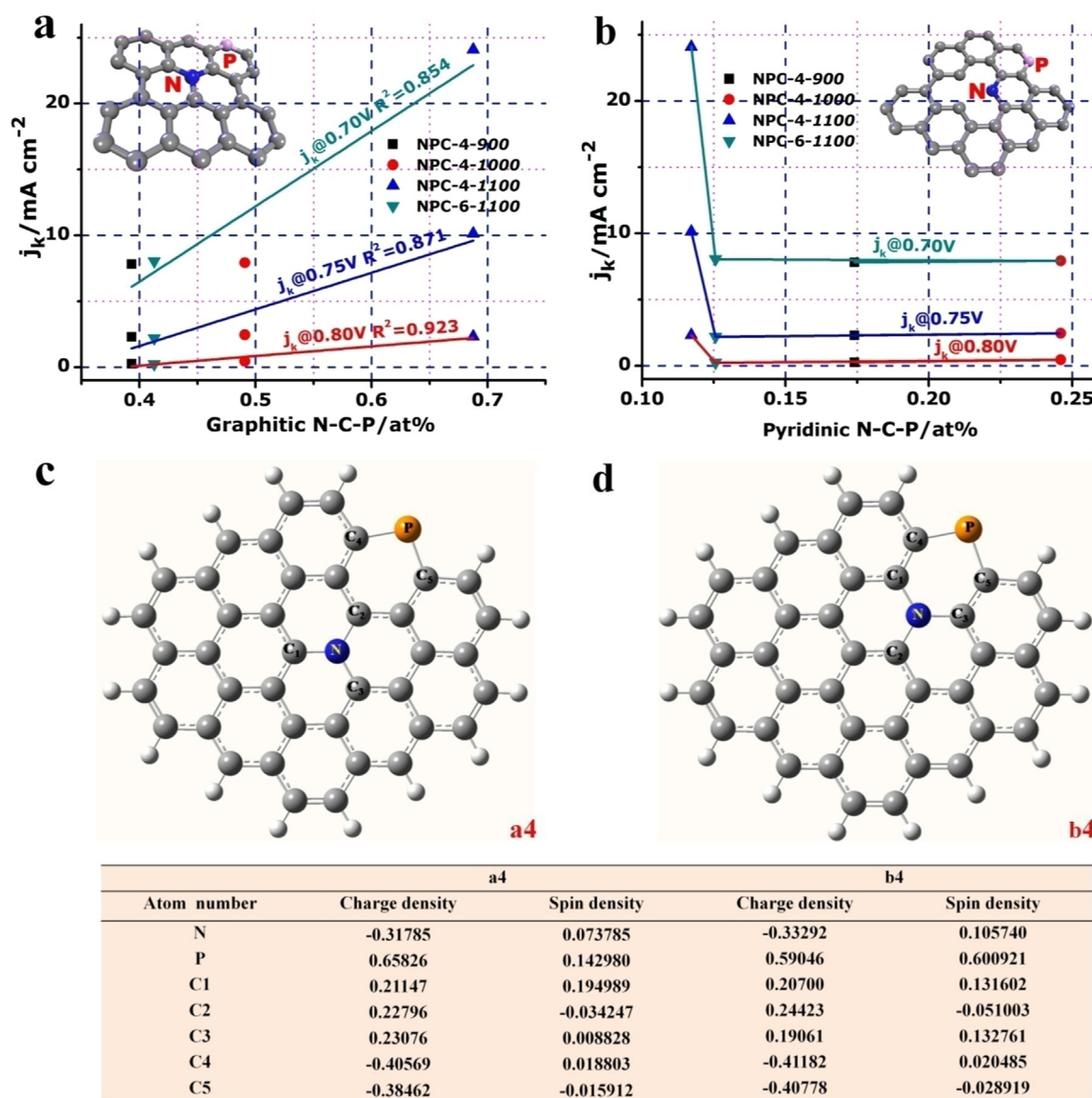


Fig. 3. Steady-state ORR polarization curves for NPC-4-*T* (a) and NPC-*X*-1100 (b) catalysts in O<sub>2</sub>-saturated 0.1 M HClO<sub>4</sub> with a scan rate of 5 mV/s and a rotation speed of 1600 rpm; (c) RDE polarization curves and peroxide yield of NPC-4-1100, NPC-4-1100-Zn and commercial Pt/C in O<sub>2</sub>-saturated 0.1 M HClO<sub>4</sub> with a scan rate of 5 mV/s and a rotation speed of 1600 rpm; (d) Tafel plots of NPC-4-1100, NPC-4-1100-Zn and Pt/C catalysts; (e) Koutecky-Levich (K-L) plots for NPC-4-1100-Zn at various potentials; (f) mass activity of ORR at different potentials on NPC-4-1100 and NPC-4-1100-Zn samples; (g, h) steady-state ORR polarization curves of NPC-4-1100-Zn (g) and Pt/C (h) before and after 10,000 potential cycles in O<sub>2</sub>-saturated 0.1 M HClO<sub>4</sub>; (i) polarization curves and corresponding power densities of membrane electrode assemblies fabricated with NPC-4-1100 and NPC-4-1100-Zn cathode catalysts.

been reported [40–42], we have reason to believe that the NPC catalysts with onset potential exceeding 0.9 V must originated from the creation of intrinsically more active sites, due to the N and P co-doping. To reveal the synergistic functions of N and P in ORR, we further studied the relationship between the current densities and the different dopants' concentration, where the graphitic N-C-P (G<sub>N</sub>-C-P) and pyridinic N-C-P (P<sub>N</sub>-C-P) species (configuration shown inset Fig. 4a, b) were majorly investigated. As shown in Fig. 4a, we found an obvious linear correlation between G<sub>N</sub>-C-P concentration and ORR activity at high potential (0.8 V), where the correlation parameter R<sup>2</sup> is calculated to be 0.923, clearly evidencing the synergistic effect between graphitic carbon and C-P bond. At lower potentials, as other active sites (such as pyridinic N-C species) became active and contribute partially to the kinetic current, decreased linear dependences are observed (R<sup>2</sup> = 0.871 @0.75 V, R<sup>2</sup> = 0.854 @0.70 V), which are however still sufficient to demonstrate the synergy effect. The critical role of G<sub>N</sub>-C-P was further confirmed by excluding current contribution of pyridinic N-C active sites according to Nakamura's work (details are shown in supporting information), which results in increased correlation coefficient to 0.886 at 0.75 V and 0.875 at 0.70 V, respectively. The specific activity per G<sub>N</sub>-C-P specie is estimated to be 0.18 e s<sup>-1</sup> at 0.8 V, much higher than that of the pyridinic N-C active site at 0.5 V (0.13 e s<sup>-1</sup>) [29], verifying the dominated role of G<sub>N</sub>-C-P active sites. In contrast, no

distinguishable correlation between the kinetic current density and P<sub>N</sub>-C-P contents is noticed (Fig. 4b), indicating that the ORR activity is determined solely by the G<sub>N</sub>-C-P concentration at high potential.

Density functional theory (DFT) calculations were performed to further reveal the real active site structure. It is known that the ORR activity of N doped carbon is rooted from the charge transfer from C to N due to the higher electron negativity of the latter, where the C atoms with positive charges results in increased ORR activity. For the NPC catalysts in the G<sub>N</sub>-C-P model, we found that the charge and/or spin density of neighboring C atoms further increases when P atoms are bonded to carbon atoms adjacent to graphitic N. On the contrary, for the P<sub>N</sub>-C-P type, the charge and spin density of the carbon atoms decrease with the introduction of neighboring P dopants, compared with the pristine N-doped carbon (Fig. 4c, d and Figs. S19–22 and Tables S4–S7). G<sub>N</sub>-C-P species are believed as the origination for the much higher intrinsic activity, consistent with the results in Fig. 4a. The possible configurations of active site structures were then confirmed by comparing the charge/spin density of various structure models. As shown in Fig. 4c, d, the optimized models were a4 and b4 due to the highest charge/spin density achieved. Specifically, the spin density was up shifted to 0.195 for C1 in Model a4 and 0.133 for C3 in Model b4 (Fig. 4c, d and Tables S4 and S5), which is higher than that of N-doped C sample (0.178 for C1 in a4 and -0.008 for C3 in b4).



**Fig. 4.** (a) correlation between kinetic current densities of ORR at 0.8, 0.75, and 0.7 V versus RHE and the graphitic N-C-P species concentrations; (b) Correlation between kinetic current densities and the pyridinic N-C-P concentrations; (c, d) spin and charge density of carbon network (gray) dual-doped by N (blue) and P (orange). C1 has very high spin density, C2 and C3 have high positive charge density, and C4 and C5 have moderately high positive spin densities. (For interpretation of the references to color in this figure legend, the reader is referred to the web version of this article.)

To confirm the more positive charge characteristics of the active C atoms, we further employed the surface-enhanced resonance Raman spectroscopy (SERRS) and used  $\text{SCN}^-$  to probe the alternation in surface resonance signals after adsorption. The peaks corresponding to P–C/P–C–N ( $620\text{--}700\text{ cm}^{-1}$ ) bond stretching modes and characteristic peaks of N–C/N–C–P species ( $770\text{ cm}^{-1}$  to  $880\text{ cm}^{-1}$ ) show significantly attenuation in peak density after adsorption, evidencing the positively charged nature of C atoms (Fig. 5a). Notably, the NPC-4-1100-Zn sample exhibits a more attenuation compared to N-doped C, suggesting more positive charge of C atoms due to N, P co-doping (Fig. 5b), being consistent with the DFT calculation results.

Last, ultraviolet photoelectron spectroscopy (UPS) measurements were carried out to investigate the doping effect of N and P on the work function of the catalysts. In Fig. 5c, two bands could be clearly distinguished, assignable to  $\sigma$  and  $\pi$  valence-band of graphite. The work functions determined from He I spectra is 4.70, 4.41, and 4.59 eV for the N-doped C, P-doped C, and NPC-4-1100-Zn, respectively (Fig. 5d). Compared to the N-doped C, the lowered local function of the NPC-4-1100-Zn catalyst suggests a lower energetic barrier (higher driving energy) for donating electrons

from the surface of the N, P co-doped catalyst to the adsorbed molecular oxygen, thereby facilitating the formation of the OOH species, which is known to be the rate-determining step in the ORR process.

#### 4. Conclusion

In summary, we addressed the intrinsic activity and the active sites unleashing issues of metal-free ORR catalysts using electronic modulation and nanostructure engineering strategy. Specifically, an onset potential of 0.91 V and a half-wave potential of 0.79 V were achieved in 0.1 M  $\text{HClO}_4$ , ranking the first among the metal-free carbon-based electrocatalysts and is comparable to the  $\text{M-N}_x\text{-C}$  catalysts. Furthermore, in-situ fuel cell test demonstrates maximum power output at  $579\text{ mW cm}^{-2}$ , the best for metal-free catalysts and even better than most  $\text{M-N}_x\text{-C}$  materials. This result provides a sound refute to the judgement that only metal containing materials are viable nonprecious catalysts in acidic solution. In-depth study on the active site structure revealed that the positive charged carbon atoms adjacent to both graphitic N and P species are the main active sites. The enhanced charge/

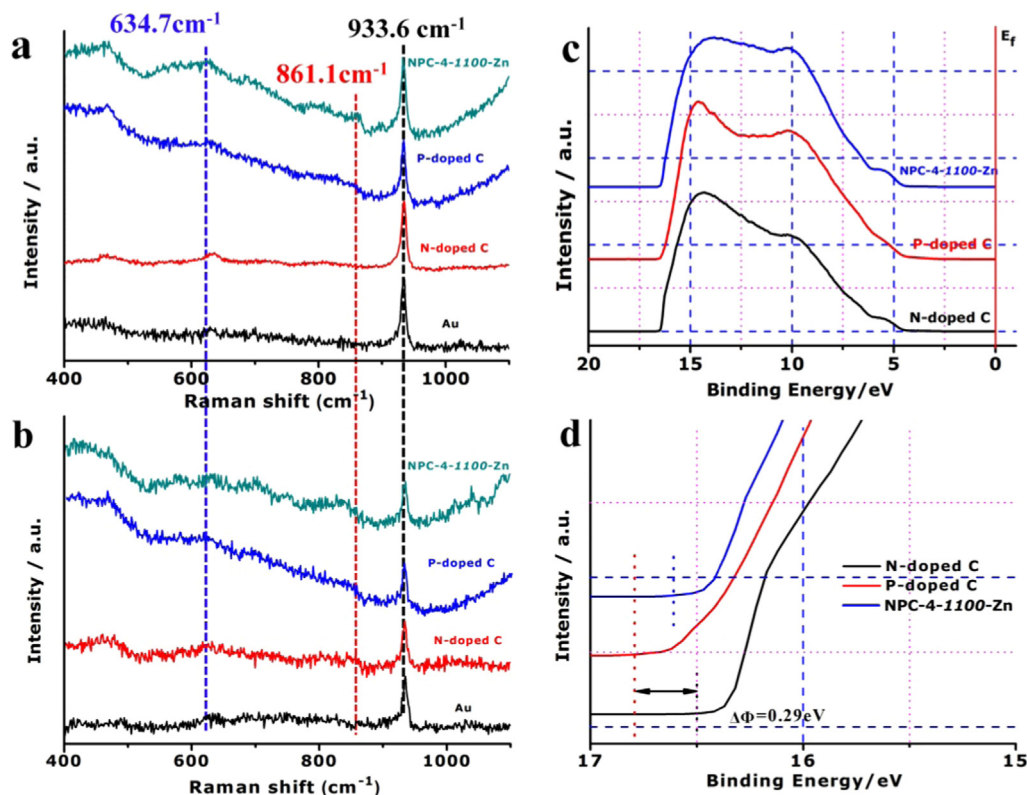


Fig. 5. (a, b) SERRS spectra of the N-doped C, P-doped C and NPC-4-1100 catalysts before (a) and after (b) injecting KSCN in 0.1 M HClO<sub>4</sub>; (c) UPS spectra collected using an He I (21.2 eV) radiation; (d) the enlarged view of the secondary electron tail threshold.

spin density and lower local work function due to co-doping were further revealed by DFT calculations and UPS measurements, respectively. Our findings provide new directions for the design of earth-abundant materials as highly active ORR electrocatalysts.

## Acknowledgments

The work is supported by the National Natural Science Foundation of China (21633008, 21433003, U1601211, 21733004), National Science and Technology Major Project (2016YFB0101202), Jilin Province Science and Technology Development Program (20150101066JC, 20160622037JC, 20170203003SF, 20170520150JH), Hundred Talents Program of Chinese Academy of Sciences and the Recruitment Program of Foreign Experts (WQ20122200077).

## Appendix A. Supporting information

Supplementary data associated with this article can be found in the online version at <http://dx.doi.org/10.1016/j.nanoen.2018.04.021>.

## References

- [1] H.A. Gasteiger, S.S. Kocha, B. Sompalli, F.T. Wagner, *Appl. Catal. B: Environ.* 56 (2005) 9–35.
- [2] J. Greeley, I.E.L. Stephens, A.S. Bondarenko, T.P. Johansson, H.A. Hansen, T.F. Jaramillo, Rossmeisl, Chorkendorff, J.K. Nørskov, *Nat. Chem.* 1 (2009) 552–556.
- [3] G. Wu, K.L. More, C.M. Johnston, P. Zelenay, *Science* 332 (2011) 443–447.
- [4] M. Lefevre, E. Proietti, F. Jaouen, J.-P. Dodelet, *Science* 324 (2009) 71–74.
- [5] K. Gong, F. Du, Z. Xia, M. Durstock, L. Dai, *Science* 323 (2009) 760–764.
- [6] D.S. Yu, E. Nagelli, F. Du, L.M. Dai, *J. Phys. Chem. Lett.* 1 (2010) 2165–2173.
- [7] L.M. Dai, Y.H. Xue, L.T. Qu, H.J. Choi, J.B. Baek, *Chem. Rev.* 115 (2015) 4823–4892.
- [8] H.B. Yang, J.W. Miao, S.F. Hung, J.Z. Chen, H.B. Tao, X.Z. Wang, L.P. Zhang, R. Chen, J.J. Gao, H.M. Chen, L.M. Dai, B. Liu, *Sci. Adv.* 2 (2016).
- [9] Z. Chen, D. Higgins, H. Tao, R.S. Hsu, Z. Chen, *J. Phys. Chem. C* 113 (2009) 21008–21013.
- [10] D. Yu, Q. Zhang, L. Dai, *J. Am. Chem. Soc.* 132 (2010) 15127–15129.
- [11] S. Yang, L. Zhi, K. Tang, X. Feng, J. Maier, K. Müllen, *Adv. Funct. Mater.* 22 (2012) 3634–3640.
- [12] Z. Lin, G.H. Waller, Y. Liu, M. Liu, C.-p. Wong, *Nano Energy* 2 (2013) 241–248.
- [13] Y. Xue, D. Yu, L. Dai, R. Wang, D. Li, A. Roy, F. Lu, H. Chen, Y. Liu, J. Qu, *Phys. Chem. Chem. Phys.* 15 (2013) 12220–12226.
- [14] R. Liu, D. Wu, X. Feng, K. Müllen, *Angew. Chem.* 122 (2010) 2619–2623.
- [15] J. Liang, X. Du, C. Gibson, X.W. Du, S.Z. Qiao, *Adv. Mater.* 25 (2013) 6226–6231.
- [16] K. Ai, Y. Liu, C. Ruan, L. Lu, G. Lu, *Adv. Mater.* 25 (2013) 998–1003.
- [17] S. Chen, J. Bi, Y. Zhao, L. Yang, C. Zhang, Y. Ma, Q. Wu, X. Wang, Z. Hu, *Adv. Mater.* 24 (2012) 5593–5597.
- [18] W. Ding, Z. Wei, S. Chen, X. Qi, T. Yang, J. Hu, D. Wang, L.-J. Wan, S.F. Alvi, L. Li, *Angew. Chem.* 125 (2013) 11971–11975.
- [19] Z. Yang, Z. Yao, G. Li, G. Fang, H. Nie, Z. Liu, X. Zhou, Xa Chen, S. Huang, *ACS Nano* 6 (2012) 205–211.
- [20] C. Zhang, N. Mahmood, H. Yin, F. Liu, Y. Hou, *Adv. Mater.* 25 (2013) 4932–4937.
- [21] L. Yang, S. Jiang, Y. Zhao, L. Zhu, S. Chen, X. Wang, Q. Wu, J. Ma, Y. Ma, Z. Hu, *Angew. Chem.* 123 (2011) 7270–7273.
- [22] X. Sun, Y. Zhang, P. Song, J. Pan, L. Zhuang, W. Xu, W. Xing, *ACS Catal.* 3 (2013) 1726–1729.
- [23] W. Ai, Z. Luo, J. Jiang, J. Zhu, Z. Du, Z. Fan, L. Xie, H. Zhang, W. Huang, T. Yu, *Adv. Mater.* 26 (2014) 6186–6192.
- [24] S. Wang, L. Zhang, Z. Xia, A. Roy, D.W. Chang, J.-B. Baek, L. Dai, *Angew. Chem. Int. Ed.* 51 (2012) 4209–4212.
- [25] Y. Zhao, L. Yang, S. Chen, X. Wang, Y. Ma, Q. Wu, Y. Jiang, W. Qian, Z. Hu, *J. Am. Chem. Soc.* 135 (2013) 1201–1204.
- [26] L. Zhang, Z. Xia, *J. Phys. Chem. C* 115 (2011) 11170–11176.
- [27] H. Kim, K. Lee, S.I. Woo, Y. Jung, *Phys. Chem. Chem. Phys.* 13 (2011) 17505–17510.
- [28] A. Ferre-Vilaplana, E. Herrero, *Phys. Chem. Chem. Phys.* 17 (2015) 16238–16242.
- [29] D. Guo, R. Shibuya, C. Akiba, S. Saji, T. Kondo, J. Nakamura, *Science* 351 (2016) 361–365.
- [30] L. Zhang, J. Niu, M. Li, Z. Xia, *J. Phys. Chem. C* 118 (2014) 3545–3553.
- [31] H.-W. Liang, X. Zhuang, S. Brüller, X. Feng, K. Müllen, *Nat. Commun.* 5 (2014) 4973.
- [32] H.-W. Liang, W. Wei, Z.-S. Wu, X. Feng, K. Müllen, *J. Am. Chem. Soc.* 135 (2013) 16002–16005.
- [33] K. Ai, Y. Liu, C. Ruan, L. Lu, G.M. Lu, *Adv. Mater.* 25 (2013) 998–1003.
- [34] Y.Z. Chen, C. Wang, Z.Y. Wu, Y. Xiong, Q. Xu, S.H. Yu, H.L. Jiang, *Adv. Mater.* 27 (2015) 5010–5016.
- [35] P.H. Matter, L. Zhang, U.S. Ozkan, *J. Catal.* 239 (2006) 83–96.
- [36] S.B. Yang, X.L. Feng, X.C. Wang, K. Mullen, *Angew. Chem. Int. Ed.* 50 (2011) 5339–5343.
- [37] J.T. Zhang, Z.H. Zhao, Z.H. Xia, L.M. Dai, *Nat. Nanotechnol.* 10 (2015) 444–452.

- [38] Z.L. Ma, S. Dou, A.L. Shen, L. Tao, L.M. Dai, S.Y. Wang, *Angew. Chem. Int. Ed.* 54 (2015) 1888–1892.
- [39] M.A. Patel, F.X. Luo, M.R. Khoshi, E. Rabie, Q. Zhang, C.R. Flach, R. Mendelsohn, E. Garfunkel, M. Szostak, H.X. He, *ACS Nano* 10 (2016) 2305–2315.
- [40] J. Shui, M. Wang, F. Du, L. Dai, *Sci. Adv.* 1 (2015) e1400129.
- [41] Q. Lai, L. Zheng, Y. Liang, J. He, J. Zhao, J. Chen, *ACS Catal.* 7 (2017), pp. 1655–1663.
- [42] Z. Liu, Q. Shi, R. Zhang, Q. Wang, G. Kang, F. Peng, *J. Power Sources* 268 (2014) 171–175.



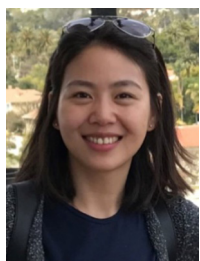
**Jianbing Zhu** received his BS from Beihang University, Beijing in 2010. He obtained his PhD degree in Physical Chemistry from Changchun Institute of Applied Chemistry, Chinese Academy of Sciences in 2016. Then he works as a postdoctoral research fellow in the University of Waterloo, and his research interests focus on the development of non-precious metal electrocatalysts for fuel cells and metal-air batteries.



**Meiling Xiao** received her BS from Nanjing Normal University, China, in 2011 and Ph. D degree in Physical Chemistry from Changchun Institute of Applied Chemistry, Chinese Academy of Sciences in 2016. Currently, she works as a postdoctoral research fellow in the University of Waterloo, now her research interests focus on the exploration of earth-abundant materials to replace noble metal materials for electrocatalytic process and the understanding of electrocatalysis mechanism on these novel electrocatalysts.



**Ping Song** received her BS from Northeast Normal University in 2005. She obtained her PhD degree in Physical Chemistry from Northeast Normal University in 2010. Then she works as a postdoctoral research fellow in the Dalian Institute of Chemical Physics, Chinese Academy of Sciences, and her research interests focus on the mechanism for fluorescent sensor. Now, she works as an associate professor in Changchun Institute of Applied Chemistry, Chinese Academy of Sciences, and her research interests focus on the development of non-precious metal electrocatalysts for fuel cells and the investigation for catalytic mechanism.



**Jing Fu** is now pursuing her Ph.D. in chemical engineering under the supervision of Prof. Zhongwei Chen at the University of Waterloo, Waterloo, Canada. Her current research interests include the development of advanced nanostructured electrode materials and solid-state electrolytes for flexible rechargeable metal-air batteries.



**Zhao Jin** received his Ph.D. degree in physical chemistry from Jilin University. He is now an associate professor in Laboratory of Advanced Power Sources, Changchun Institute of Applied Chemistry, Chinese Academy of Sciences. His research interest focuses on design, synthesis and characterization of electrocatalysts include metal nanoparticle and metal-organic complex for oxygen reduction, methanol oxidation, H<sub>2</sub> evolution and O<sub>2</sub> evolution, as well as preparation of MEA and performance evaluation of PEMFC.



**Liang Ma** had earned his PhD degree in Changchun Institute of Applied Chemistry, Chinese Academy of Sciences on 2011. During 2011–2013, he worked as a postdoctoral fellow in Indiana University-Purdue University, Indianapolis. Later, He moved to National University of Singapore as a research fellow from 2013 to 2014. He is now working as an associate professor in Faculty of Materials Science and Chemistry, China University of Geosciences. His research focuses on developing key materials for low temperature direct liquid fuel cell and developing earth-abundant transition metal compounds for water electrolysis and CO<sub>2</sub> electroreduction.



**Junjie Ge** received her Ph.D in physical chemistry from Chinese Academy of Sciences in 2010. She worked at University of South Carolina and University of Hawaii as a postdoc fellow for almost 5 years. She joined Changchun Institute of Applied Chemistry in 2015 as a professor, where she was recruited in the Hundred Talents Program in CAS (2015). Her research interests comprehend fuel cells, nanoscience, catalysis, and electrochemistry. She has published 30 + peer-reviewed papers and several posters, abstracts and presentations at international conferences. She is also acting as a referee for several top journals in the field related to electrochemistry and fuel cells.



**Changpeng Liu** received his Ph.D. in Physical Chemistry in 2002 and was appointed as professor at CIAC in 2006. He has been in charge of and taken part in several relevant fuel cells projects (e.g. 863 programs and 973 programs China). Liu's research focuses on the technology and performances of catalysts, electrodes/MEA and stacks.



**Dr. Zhongwei Chen** is Canada Research Chair Professor in Advanced Materials for Clean Energy at the University of Waterloo, the Fellow of the Canadian Academy of Engineering and Vice President of International Academy of Electrochemical Energy Science (IAOEEES). His research interests are in the development of advanced energy materials and electrodes for fuel cells, metal-air batteries, and lithium-ion batteries. He has published 2 book, 9 book chapters and more than 220 peer reviewed journal articles with over 13,000 citations with a H-index of 57. He is also listed as inventor on 15 US/international patents, with several licensed to companies in USA and Canada.



**Prof. Wei Xing** is currently director of Clean Energy Laboratory in Changchun Institute of Applied Chemistry (CIAC), Chinese Academy of Sciences. After receiving his Ph.D. in Physical Chemistry, at CIAC in 1995, he worked at Hong Kong Productivity Council (HKPC), research in electrochemical treatment of metal surface. In 2001, he joined in CIAC as a professor and devoted to the development of advanced chemical power sources. He has published over 100 papers in peer-reviewed journals and applied over 30 patents. His research areas currently involve proton exchange membrane fuel cell from fundamental electro-catalytic process to relevant fuel cell assemble and test.